PHYSICAL REVIEW A **88**, 043417 (2013)

High-order-harmonic generation from Rydberg states at fixed Keldysh parameter

E. A. Bleda,[1] I. Yavuz,[2] Z. Altun,[2] and T. Topcu[3,4]

[1]*Department of Mathematics and Computer Science, Istanbul Arel University, 34537 Buyukcekmece, Istanbul, Turkey*

[2]*Department of Physics, Marmara University, 34722 Ziverbey, Istanbul, Turkey*

[3]*Department of Physics, Auburn University, Alabama 36849-5311, USA*

[4]*Department of Physics, University of Nevada, Reno, Nevada 89557, USA*

(Received 23 August 2013; published 15 October 2013)

Because the commonly adopted viewpoint that the Keldysh parameter γ determines the dynamical regime in strong field physics has long been demonstrated to be misleading, one can ask what happens as relevant physical parameters, such as laser intensity and frequency, are varied while γ is kept fixed. We present results from our one- and fully three-dimensional quantum simulations of high-order-harmonic generation (HHG) from various bound states of hydrogen with n up to 40, where the laser intensities and the frequencies are scaled from those for $n = 1$ in order to maintain a fixed Keldysh parameter $\gamma < 1$ for all n. We find that as we increase n while keeping γ fixed, the position of the cutoff scales in a well-defined manner. Moreover, a secondary plateau forms with a new cutoff, splitting the HHG plateau into two regions. The first of these subplateaus is composed of lower harmonics, and has a higher yield than the second one. The latter extends up to the semiclassical $I_p + 3.17U_p$ cutoff. We find that this structure is universal, and the HHG spectra look the same for all $n \gtrsim 10$ when plotted as a function of the scaled harmonic order. We investigate the n, l, and momentum distributions to elucidate the physical mechanism leading to this universal structure.

DOI: 10.1103/PhysRevA.88.043417 PACS number(s): 32.80.Rm, 42.65.Ky, 32.80.Ee

I. INTRODUCTION

High-order-harmonic generation (HHG) is a nonlinear phenomenon in which atoms interacting with an intense laser pulse emit photons whose frequencies are integer multiples of the driving laser frequency. The emphatic motivation is the generation of spatially and temporally coherent bursts of attosecond pulses with high frequencies covering a range from vacuum ultraviolet (VUV) to the soft x-ray region [1]. Filtering the high-frequency part of a high-harmonic spectrum allows the syntheses of ultrashort, coherent light pulses with energies in the extreme ultraviolet (XUV) part of the spectrum. This allows for tracing and controlling electronic processes in atoms, as well as coupled vibrational and electronic processes in molecules [2,3]. Some of the most visible applications of ultrashort pulses of attosecond duration involve resolving the electronic structure with high degree of spatial and temporal resolution [4], controlling the dynamics in the XUV-pumped excited molecules [5], and exciting and probing inner-shell electron dynamics with high resolution [6]. Time-resolved holography [7], imaging of molecular orbitals [3], and attosecond streaking [8] are also among the state-of-the-art applications of HHG.

High-order-harmonic generation is a process well described within the semiclassical three-step model (ionization, propagation, followed by recombination). The plateau region, where consecutive harmonics have approximately the same intensity, constitutes the main body of a high-harmonic spectrum. The first step of the three-step model is the tunneling of the electron through the Coulomb potential barrier suppressed by the laser field. The second step is laser-driven propagation of the free electron, and the third step is the rescattering of the electron with its parent ion. During this last step, the electron can recombine with its parent ion and liberate its excess energy as a short wavelength harmonic photon. The three-step model predicts that the highest kinetic energy that an electron gains during its laser-driven excursion is given by $3.17U_p$, where $U_p = F^2/(4\omega_0^2)$ is the quiver energy of the free electron in the laser field, and F and ω_0 are the laser field amplitude and frequency. The highest harmonic frequency, ω_c, that can be generated within this model is $q_{\max}\omega_0 = |E_b| + 3.17U_p$, where $|E_b|$ is the binding energy of electron in the atom and $q_{\max}$ is the order of the cut-off harmonic [9].

A crucial assumption in this physical picture is that the electron tunnels into the continuum in the first step in a laser field characterized by a small Keldysh parameter. This liberates the electron with no excess kinetic energy, and its subsequent excursion is driven by the classical laser field alone. Keldysh parameter γ is commonly used to refer to one of the two dominant ionization dynamics in strong fields: tunneling or multiphoton regimes [10]. It is defined as the the time it takes for the electron to tunnel the barrier in units of the laser period, i.e., $\gamma \sim \tau/T$. Here τ is the tunneling time and $T = 2\pi/\omega_0$ is the laser period. If the tunneling time is much smaller than the laser period, one could expect that it is likely for the electron to tunnel through the barrier. In contrast, if tunneling time is much longer than the laser period, then the electron does not have enough time to tunnel through the depressed Coulomb barrier, and ionization can only occur through photon absorption. The Keldysh parameter can be expressed as $\gamma = \omega_0\sqrt{2|E_b|}/F$ [10].

Although the Keldysh parameter is widely used to refer to the underlying dynamics in strong field ionization, there are studies which suggest that it is an inadequate parameter in making this assessment [11–13] when a large range of laser frequencies is considered. Thus, it is natural to ask what happens in the strong field ionization step of HHG as a function of n, as relevant parameters, such as laser intensity and frequency, are varied while γ is kept fixed. In this paper, we investigate the HHG process from the ground and the Rydberg states of a hydrogen atom using a one-dimensional

s-wave model supported by fully three-dimensional quantum simulations. The central idea is that in a hydrogen atom, both the field strength F and the frequency ω_0 scale in a particular fashion with the principal quantum number n. Scaling the field strength by $1/n^4$ and the frequency by $1/n^3$, it is evident that $\gamma = \omega_0\sqrt{2\,|E_b|}/F$ remains unaffected as n is changed, provided that both F and ω_0 are scaled accordingly while n is varied.

In the spirit of the Keldysh theory, going beyond the ground state and starting from higher n as the initial state, scaling F and ω_0 to maintain a fixed value of γ should keep the ionization step of the harmonic generation in the same dynamical regime. We calculate HHG spectra starting from the ground state of hydrogen using laser parameters for which $\gamma < 1$ (tunneling), and then calculate the high-harmonic spectra from increasingly larger n states, scaling F and ω_0 from the ground-state simulations and keep γ fixed. If the Keldysh parameter is indeed adequate in referring to the ionization step properly in HHG, one should expect that the physics of the three-step process would remain unchanged, as the remainder of the steps involve only classical propagation of the electron in the continuum, and the final recombination step, which is governed by the conservation of energy.

There are a number of studies devoted to HHG from Rydberg atoms. The main motivation in these efforts is primarily increasing the conversion efficiency in the harmonic generation to obtain higher yields, which in turn would enable the generation of more intense attosecond pulses. Hu *et al.* [14] demonstrated that, by stabilization of the excited outer electron of the Rydberg atom in an intense field, a highly efficient harmonic spectrum could be generated from the more strongly bound inner electrons. In another recent study, Zhai *et al.* [15,16] proposed that an enhanced harmonic spectrum is possible if the initial state is prepared as a superposition of the ground and the first excited state. The idea behind this method is that when coupled with the ground state, ionization can occur out of the excited state, initiating the harmonic generation. Since the excited state has lower ionization potential than the ground state, this in principle can result in higher conversion efficiency if the electron subsequently recombines into the excited state. In this scenario, the high-harmonic plateau would still cut off at the semiclassical limit $I_p + 3.17U_p$ with I_p being that of the excited state. If, however, upon ionization out of the excited state, the electron recombines into the ground state, the cutoff can be pushed up to higher harmonics. The same principle is also at play in numerous studies proposing two-color driving schemes for HHG, with one frequency component serving to excite the ground state up to an excited level with a lower ionization potential, thus increasing the ionization yield (see, for example, [17]).

In this paper, we report HHG spectra from ground and various Rydberg states with n up to 40 for hydrogen atom, where the laser intensity and the frequency are such that the ionization step occurs predominantly in the tunneling regime. Starting with $\gamma = 0.755$ at $n = 1$, we go up in n of the initial state and scale F by $1/n^4$ and ω_0 by $1/n^3$, keeping γ constant. We discuss the underlying mechanism in terms of field ionization and final n distributions after the laser pulse. We find that the harmonic order of the cutoff predicted by the semiclassical three-step model scales as $1/n$ when F and ω_0 are scaled as described above, and γ is kept fixed. We repeat some of these model simulations by solving the fully three-dimensional time-dependent Schrödinger equation to investigate the effects which may arise due to angular momenta in high-n manifolds. For select initial n states, we look at momentum distributions of the ionized electrons, and the wave function extending beyond the peak of the depressed Coulomb potential at $1/\sqrt{F}$. Unless otherwise stated, we use atomic units throughout.

II. ONE-DIMENSIONAL CALCULATIONS

The time-dependent Schrödinger equation of an electron interacting with the proton and the laser field $F(t)$ in the s-wave model in length gauge reads

$$i\frac{\partial\psi(r,t)}{\partial t} = \left[-\frac{1}{2}\frac{d^2}{dr^2} - \frac{1}{r} + rF(t)\right]\psi(r,t). \tag{1}$$

In our simulations, time runs from $-t_f$ to t_f. This choice of time range centers the carrier envelope of the laser at $t = 0$, which simplifies its mathematical expression. We choose the time dependence of the electric field $F(t)$ to be

$$F(t) = F_0 \exp[-(4\ \ln\ 2)t^2/\tau^2]\cos(\omega_0 t), \tag{2}$$

where F_0 is the peak field strength, ω_0 is the laser frequency, and τ is the field duration at FWHM. Our one-dimensional model is an s-wave model and is restricted to the half space $r \geqslant 0$ with a hard wall at $r = 0$. Having a hard wall at $r = 0$ when there is no angular momentum can potentially be problematic, because the electron can absorb energy from the hard wall when using $-1/r$ potential. However, we believe that this model is adequate for the problem at hand, because we are deep in the tunneling regime. In our calculations, the number of photons required for ionization to occur through photon absorption is $\sim$9 for $n = 1$, approaches 71 by $n = 10$, and stays so for higher n. As a result, ionization takes place primarily in the tunneling regime. If an extra photon is absorbed at the hard wall, its effect would mostly concern the lowest harmonics, which we are not interested in. In Sec. III, we show that the results we obtain in this section are consistent with our findings from fully three-dimensional calculations.

We consider cases in which the electron is initially prepared in an ns state, where n ranges from 1 up to 40. Our pulse duration is four cycles at FWHM for each case, and the wavelength of the laser field is 800 nm for the ground state. This gives a 2.7 fs optical cycle when the wavelength is 800 nm. Thus, the total pulse duration τ for the ground state is $\sim$11 fs and it scales as n^3. For the $4s$ state, this results in a pulse duration of $\sim$704 fs, while it amounts to $\sim$5.6 ps for the $8s$ state.

For the numerical solution of Eq. (1), we perform a series of calculations to make sure that the mesh and box size of the radial grid and the time step we use are fine enough so that our results are converged to within a few percent. As we go beyond the $1s$ state, we increase the radial box size to accommodate the growing size of the initial state and the interaction region. We propagate Eq. (1) for excited states using a square-root mesh of the form $j^2\delta r$, where j is the index of a radial grid point, $\delta r = R/N^2$, R is the box size, and N is the number of grid points. This type of grid is more

efficient than using a uniform mesh in problems involving Rydberg states [18], because it puts roughly the same number of points between the successive nodes of a Rydberg state. For the ground state, the box size is $R = 750$ a.u. and $N = 800$, which gives $\delta r = 0.0012$ a.u. For excited states, the box size grows $\sim n^2$ and with a proper selection of δr, we make sure that the dispersion relation $k\delta r = 0.5$ holds for each n state, where k is the maximum electron momentum acquired from the laser field: $k = \sqrt{2E_{\max}}$ and $E_{\max} = 3.17U_p$.

The time propagation of the wave function is carried out using an implicit scheme. For the temporal grid spacing δt, we use $n^3/180$ of a Rydberg period, which is small enough to give converged results. A smooth mask function which varies from 1 to 0 starting from 2/3 of the way between the origin and the box boundary is multiplied with the solution of Eq. (1) at each time step to avoid spurious reflections from the box boundaries.

The time-dependent solutions of Eq. (1) are obtained for each initial ns state, which we then use to calculate the time-dependent dipole acceleration, $a(t) = \langle \ddot{r} \rangle(t)$:

$$a(t) = -\langle \psi(r,t)|[H,[H,r]]|\psi(r,t)\rangle. \tag{3}$$

Because the harmonic power spectrum is proportional to the Fourier transform of the squared dipole acceleration, we report $|a(\omega)|^2$ for harmonic spectra.

The initial wave function is normalized to unity, and the time-dependent ionization probability is calculated as the remaining norm inside the spatial box at a given time t,

$$P(t) = 1 - \int_0^R |\psi(r,t)|^2 dr. \tag{4}$$

In evaluation of the ionization probability, we propagate the wave function long enough after the pulse is turned off until $P(t)$ converges to a time-independent value.

A. Results and discussion

In our one-dimensional simulations, we consider cases where the atom is initially in an ns state with n up to 40. The laser parameters are critically chosen so that the Keldysh parameter is fixed at $\gamma = 0.755$ for each initial n, and the scaled frequency of the laser field is $\omega_0 n^3 \ll 1$, i.e., the electric field has a slowly varying time dependence compared with the Kepler period $T_K = 2\pi n^3$ of the Rydberg electron. For example, for an 800 nm laser, an optical cycle is $\sim$18 times the Kepler period for $n = 1$. The cut-off frequency ω_c predicted by the three-step model is $\omega_c = |E_b| + 3.17U_p$ [9], where $U_p = F^2/4\omega_0^2$ is the ponderomotive potential. Since $|E_b|$, F, and ω_0 scale as n^{-2}, n^{-4}, and n^{-3}, respectively, the cut-off frequency ω_c scales as n^{-2} and the harmonic order of the cutoff $q_{\max} = \omega_c/\omega_0$ scales as n for fixed γ.

Harmonic spectra from these simulations are seen in Figs. 1(a)–1(d) as a function of the scaled harmonic order $\widetilde{q} = q/n$, where $q = \omega/\omega_0$ is the harmonic order. In Fig. 1(a), the scaled laser intensity and the wavelength are $200/n^8$ TW/cm^2 and $800n^3$ nm, which correspond to $\gamma = 0.755$. The most prominent feature in these spectra is a clear double plateau structure, exhibiting one plateau with a higher yield and another following with lower yield. The second plateau terminates at the usual semiclassical cutoff. These plateaus are connected with a secondary cutoff, which converges to a fixed scaled harmonic order $\widetilde{q} = q/n$ as n becomes large.

We also note that the overall size of $|a(\omega)|^2$ drops significantly with increasing n in Fig. 1(a). For example, going from $n = 2$ to $n = 4$, $|a(\omega)|^2$ drops about three orders of magnitude, and from $n = 4$ to $n = 8$ it drops roughly four orders of magnitude. The spectrum obtained for $n = 8$ is about nine orders of magnitude lower than that for $n = 1$. Beyond $n = 8$, the overall sizes of the spectra are too small and plagued by numerical errors, which is why we stop at $n = 8$ in panel (a). This is because the amplitude of the wave function component contributing to the three-step process is too small to yield a meaningful spectrum within our numerical precision. In order to ensure sizable HHG spectra while climbing up higher in n, we adopt the following procedure: We split the Rydberg series into different groups of initial n states, which are subject to different laser parameters but have the same γ value within themselves. Within each group, we climb up in n by scaling the laser parameters for the lowest n in the group until $|a(\omega)|^2$ becomes too small. We then move onto the next group of n states, increasing the laser intensity and the frequency ($\gamma \propto \omega/F$) for the lowest n in the group while attaining the same γ as in the previous n groups. Scaling this intensity and frequency, we continue to climb up in n until again $|a(\omega)|^2$ becomes too small, at which point we terminate the group and move onto the next.

Following this procedure, we are able to achieve HHG spectra for states up to $n = 40$ in Fig. 1. The first n group in panel (a) includes states between $n = 1$–8, and the laser intensity and wavelength are $200/n^8$ TW/cm^2 and $800n^3$ nm. In panel (b) is the second group with $n = 10$–18 and the laser parameters $300/n^8$ TW/cm^2 and $652n^3$ nm. In panel (c), $n = 20$–28 and the laser parameters are $400/n^8$ TW/cm^2 and $566n^3$ nm, and finally in panel (d), $n = 30$–40 with intensity and wavelength $470/n^8$ TW/cm^2 and $522n^3$ nm. The peak field strengths corresponding to these intensities are lower than the critical field strengths for above-the-barrier ionization for the states we consider, and the ionization predominantly takes place in the tunneling regime.

The dipole accelerations at the two cut-off harmonics for each n group seen in Figs. 1(a)–1(d) are plotted in the upper two panels of Fig. 2. Here, we plot $|a(\omega)|^2$ as a function of n. This figure points to a situation in which $|a(\omega)|^2$ drops with increasing n within each group of n. Also, for the first few n groups, $|a(\omega)|^2$ drops much faster compared to those involving higher n. The reason for the decreasing $|a(\omega)|^2$ within each n group in Fig. 2, can be understood by calculating the ionization probabilities in each case, and examining how it changes as n is varied.

Although completely ionized electrons do not contribute to the HHG process, ionization and HHG are two competing processes in the tunneling regime. As a result, decrease in one alludes to decrease in the other. The ionization probabilities from the ns states in Fig. 1 are plotted against their principal quantum numbers in the lowest panel of Fig. 2. It is clear that as we go beyond the ground state, the ionization probabilities drop significantly as n is increased within each group. This decrease is rather sharp for the first group and it levels off as we go to successive groups involving higher n. The values of the scaled frequencies $\Omega = \omega n^3$ are the same in each n group, and

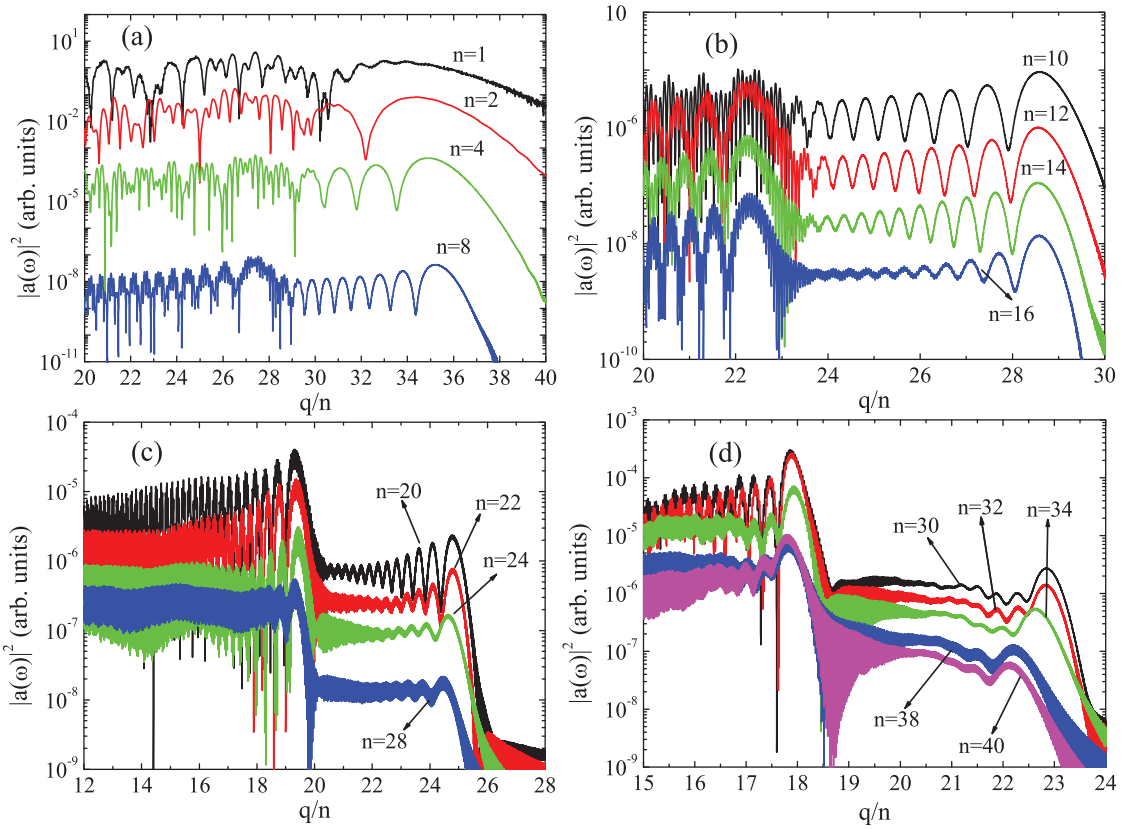

FIG. 1. (Color online) High-harmonic spectrum from the Rydberg states of the H atom. The scaled laser field intensities and the wavelengths are (a) $200/n^8$ TW/cm^2 and $800n^3$ nm, (b) $300/n^8$ TW/cm^2 and $652n^3$ nm, (c) $400/n^8$ TW/cm^2 and $566n^3$ nm, and (d) $470/n^8$ TW/cm^2 and $522n^3$ nm. The width of the laser pulse is four cycles at FWHM, and the selected parameters correspond to $\gamma = 0.755$ in each case. The scaled harmonic order is q/n, where $q = \omega/\omega_0$ is the harmonic order.

the laser parameters are chosen so as to make sure the condition $\Omega \ll 1$ holds. This ensures that the ionization is not hindered by processes such as dynamic localization. The reason behind the decreasing ionization probabilities within each n group can be understood using the quasiclassical formula [10] for the tunneling ionization rate:

$$\Gamma_K \propto (|E_b|F^2)^{1/4} \exp[-2(2|E_b|)^{3/2}/3F]. \quad (5)$$

The laser field intensity and electron binding energy scale as $\sim 1/n^4$ and $\sim 1/n^2$. Thus, the exponent in the exponential factor in Γ_K scales as $1/n$, which results in decreasing ionization probabilities within each n group when plotted as a function of n in the lowest panel of Fig. 2. This behavior is reflected in the corresponding HHG spectra in Fig. 1 and the upper panels in Fig. 2 as diminishing of the HHG yield.

The decrease in the ionization probability also slows down as as we successively move onto groups of higher n, as indicated by the decreasing slopes of the ionization probabilities in Fig. 2 between successive n groups. We find that the ratio of the ionization probabilities between the $2s$ and $4s$ states in Fig. 2 is $\sim$39, whereas between the $12s$ and $14s$ states it is $\sim$7, between $22s$ and $24s$ states $\sim$3, and between $32s$ and $34s$ states $\sim$2. This is an artifact of the scheme we employ in which we divide up the Rydberg series into successive groups of ns states to ensure sizable HHG spectra. The rate of decrease in the ionization probability in each group is determined by the slope of Γ_K, i.e., $d\Gamma_K/dn$. This slope is proportional to the laser intensity we pick for the lowest n in each group in order to initiate it, and we scale it down by $1/n^8$ inside the group to keep γ fixed. However, although this start-up intensity for each group is larger than what it would have been if we were to continue up in n in the previous group, it is still smaller than the initial intensity in the previous group. This results in a decreased slope going through successive n groups. Hence the decay rates for the ionization probability in successive groups taper off, which is reflected in the two upper panels in Fig. 2.

We also calculate the final n distributions for the atom after the laser pulse to see the extent of n mixing which may have occurred during its evolution in the laser field. This is done by allowing the wave functions to evolve according to Eq. (1) long enough after the laser pulse to attain a steady state. We then project them onto the bound eigenstates of the atom to determine the final probability distributions $P(n)$ to find the atom in a given bound state. The results are shown in Fig. 3. It is evident from the figure that most of the wave function resides in the initial state after the laser pulse, and that there is a small amount of mixing into adjacent n states. The mixing is small because only a small fraction of the total wave function takes part in the HHG process. However, we cannot deduce from our calculations what fraction of the wave function actually participates in HHG, and hence what fraction of it spreads to higher n. Because the HHG and ionization are competing

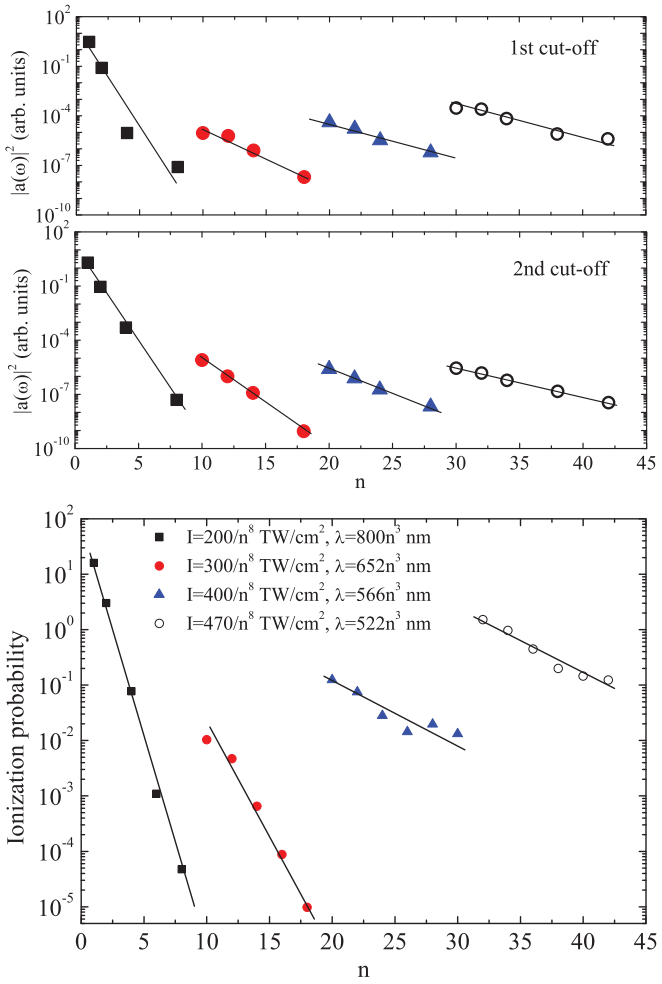

FIG. 2. (Color online) Upper two panels: $|a(\omega)|^2$ at the first and second cutoffs of the H atom as a function of n, obtained from Figs. 1(a)–1(d). Within each n group, the $|a(\omega)|^2$ drops with increasing n. (Lower panel) Ionization probabilities of the H atom as a function of n mimic the behavior of $|a(\omega)|^2$ in the upper panels. The field parameters are the same as in Figs. 1(a)–1(d).

processes in this regime, the ionization probabilities seen in the bottom panel of Fig. 2 can be taken to be an indication of the amplitude that goes into the HHG process. For example, at $n = 4$, the ionization probability is at ∼10% level in Fig. 2 and the largest amplitude after the laser pulse is in $n = 5$ in Fig. 3 at 10^{-5} level. This indicates that roughly a part in 10^6 of the amplitude participating in the HHG process recombines into higher n states. On the other hand, at $n = 20$, the ionization probability is also at ∼10% level, but the spreading in n is between ∼1% and ∼0.1% level, suggesting that between roughly 1% and 10% of the wave function participating in the HHG process gets spread over adjacent n. In the recombination step of the HHG process, the probability for recombination back into the initial state is the largest, chiefly because the electron leaves the atom through tunneling with no excess kinetic energy. It largely retains the character of the initial state because its subsequent excursion in the laser field is classical and mainly serves for the electron wave packet to acquire kinetic energy before recombination. In the next section, we discuss how this small spread helps shape the double plateau structure seen in Fig. 1.

III. THREE-DIMENSIONAL CALCULATIONS

Three-dimensional quantum calculations were carried out by solving the time-dependent Schrödinger equation as described in Ref. [18]. For the sake of completeness, we briefly outline the theoretical approach below. We decompose the time-dependent wave function in spherical harmonics $Y_{\ell,m}(\theta,\phi)$ as

$$\Psi(\vec{r},t) = \sum_{\ell} f_\ell(r,t) Y_{\ell,m}(\theta,\phi) \tag{6}$$

such that the time dependence is captured in the coefficient $f_\ell(r,t)$. For each angular momenta, $f_\ell(r,t)$ is radially represented on a square-root mesh, which becomes a constant-phase mesh at large distances. This is ideal for description of Rydberg states on a radial grid since it places roughly the same number of radial points between the nodes of high-n states. On a square-root mesh, with a radial extent R over N points, the radial coordinates of points are $r_j = j^2\delta r$, where $\delta r = R/N^2$. We regularly perform convergence checks on the number of angular momenta we need to include in our calculations as we change relevant physical parameters, such as the laser intensity. For example, $\delta r = 4 \times 10^{-4}$ a.u. in a $R = 2000$ a.u. box gave us converged results for $n = 4$, whereas $\delta r = 8 \times 10^{-4}$ a.u. in a $R = 2800$ a.u. box was sufficient at $n = 8$. We also found that the number of angular momenta we needed to converge the harmonic spectra was much larger than $n - 1$ for an initial n state (e.g., ∼120 for the $n = 8$ state).

We split the total Hamiltonian into an atomic Hamiltonian plus the interaction Hamiltonian, such that $H(r,l,t) = H_{\rm A}(r,l) + H_{\rm L}(r,t) - E_0$. Note that we subtract the energy of the initial state from the total Hamiltonian to reduce the phase errors that accumulate over time. The atomic Hamiltonian $H_{\rm A}$ and the Hamiltonian describing the interaction of the atom with the laser field in the length gauge are

$$H_{\rm A}(r,l) = -\frac{1}{2}\frac{d^2}{dr^2} - \frac{1}{r} + \frac{l(l+1)}{2r^2}, \tag{7}$$

$$H_{\rm L}(r,t) = F(t) z \cos(\omega t). \tag{8}$$

Contribution of each of these pieces to the time evolution of the wave function is accounted through the lowest order split operator technique. In this technique, each split piece is propagated using an implicit scheme of order δt^3. A detailed account of the implicit method and the split operator technique employed is given in Ref. [18]. The interaction Hamiltonian $F(t)r\cos(\theta)$, couples ℓ to $\ell \pm 1$. The laser pulse envelope has the same time dependence as in the one-dimensional s-wave model calculations [Eq. (2)].

The harmonic spectrum is usually described as the squared Fourier transform of the expectation value of the dipole moment $[d_z(t) = \langle z \rangle(t)]$, dipole velocity $[v_z(t) = \langle \dot{z} \rangle(t)]$, or the dipole acceleration $[a_z(t) = \langle \ddot{z} \rangle(t)]$ (see [19], and references therein). In our three-dimensional calculations, we evaluate all three forms and compare them for different initial

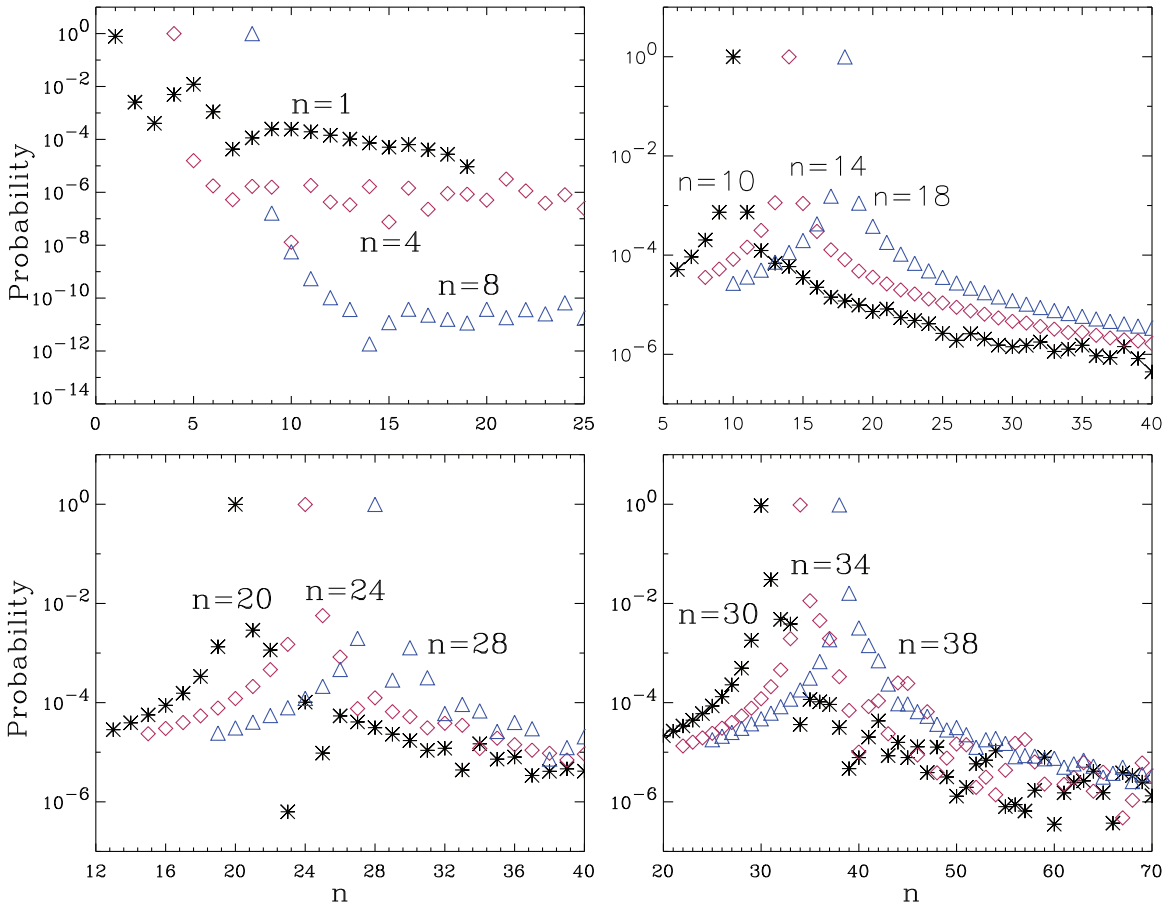

FIG. 3. (Color online) The probability distributions in n following the laser pulse for the initial states seen in Fig. 1. It is clear that the atom essentially resides in its initial state after the pulse, which means the recombination step in the harmonic generation process occurs primarily back to the initial state. The probability to find the atom in other nearby states is orders of magnitude smaller, and the probability distribution becomes symmetrical about the initial state for $n > 10$ due to decreasing anharmonicity in the surrounding energy level structure.

n states:

$$d_z(t) = \langle \Psi(\vec{r},t)|z|\Psi(\vec{r},t)\rangle, \tag{9}$$

$$v_z(t) = \langle \Psi(\vec{r},t)|\dot{z}|\Psi(\vec{r},t)\rangle, \tag{10}$$

$$a_z(t) = \langle \Psi(\vec{r},t)|\ddot{z}|\Psi(\vec{r},t)\rangle, \tag{11}$$

where $\dot{z} = -i[H,z]$ and $\ddot{z} = -[H,[H,z]]$. Reference [19] found that the Fourier transforms $d_z(\omega)$, $v_z(\omega)$, and $a_z(\omega)$ are in good agreement when the pulses are long and "weak" in harmonic generation from the ground state of the H atom, where "weak" refers to intensities below over-the-barrier ionization limit. As we increase the initial n in our simulations keeping the Keldysh parameter γ constant, we find that the agreement between these three forms of harmonic spectra gets better. This observation is in agreement with the findings in Ref. [19], because to keep γ fixed, we scale the pulse duration by $\sim n^3$ and the peak laser field strength by $\sim 1/n^4$. Although the energy of the initial state is also scaled by $\sim 1/n^2$ and the pulse duration is the same in number of optical cycles, the ionization probability drops within a given n series in Fig. 2. This suggests that the pulse is effectively getting weaker as we increase n for fixed γ. We report only the dipole acceleration form $|a_z(\omega)|^2$ to refer to harmonic spectra, chiefly because it is this form that is directly proportional to the emitted power, i.e., $S(\omega) = 2|a_z(\omega)|^2/(3\pi c^3)$.

Because high-order-harmonic generation and ionization are competing processes in the physical regime we are interested in, it is useful to investigate the momentum distribution of the ionized part of the wave function to gain further insight into the HHG process. In order to evaluate the momentum distributions, we follow the same procedure outlined in Ref. [20]. For the sake of completeness, we briefly describe the method: In all simulations, the ionized part of the wave function is removed from the box every time step during the time propagation, in order to prevent unphysical reflections from the radial box edge. This is done by multiplying the wave function by a mask function $m(r)$ at every time step, where $m(r)$ spans 1/3 of the radial box at the box edge. We retrieve the removed part of the wave function by evaluating

$$\Delta\psi_l(r,t') = [1 - m(r)]\ \psi_l(r,t') \tag{12}$$

at every time step, and Fourier transform it to get the momentum space wave function $\Delta\phi(p_\rho,p_z,t')$,

$$\Delta\phi(p_\rho,p_z,t') = 2\sum_l (-i)^l Y_{l,m}(\theta,\varphi)\int_0^\infty j_l(pr)\Delta\psi_l(r,t')r^2dr. \tag{13}$$

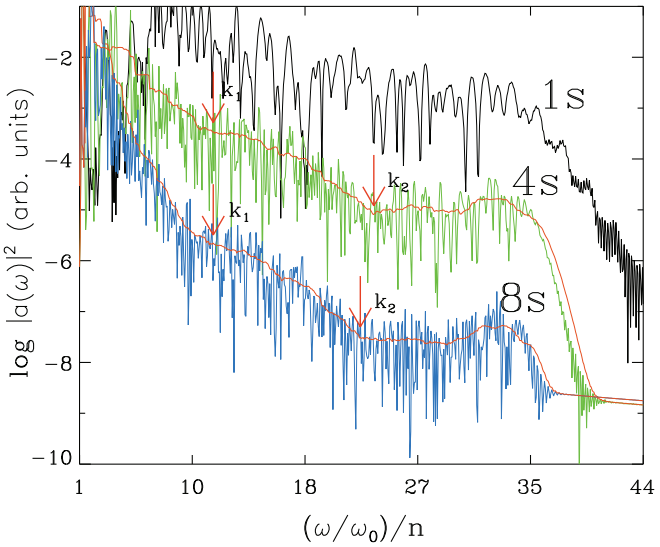

FIG. 4. (Color online) Dipole acceleration from direct solution of the three-dimensional time-dependent Schrödinger equation when the atom is initially prepared in $1s$, $4s$, and $8s$ states of the H atom. The horizontal axis is the scaled harmonic order $\widetilde{q} \equiv q/n = (\omega/\omega_0)/n$. There are three universal cut-off points in the spectra marked as k_1, k_2, and the usual $I_p + 3.17U_p$ limit. The double plateau structure mirrors that of the one-dimensional spectra from Fig. 1, with a universal secondary cutoff at $\widetilde{q} = 23.45$. The arrows marked as k_1 and k_2 are discussed in the context of Fig. 7.

Here the momentum $p = (p_\rho^2 + p_z^2)^{1/2}$ is in cylindrical coordinates and $j_l(pr)$ are the spherical Bessel functions. We then time propagate $\Delta\phi(p_\rho, p_z, t')$ to a later final time t using the semiclassical propagator

$$\Delta\phi(p_\rho, p_z, t) = \Delta\phi(p_\rho, p_z, t')e^{-iS}, \tag{14}$$

where S is the classical action. For the time-dependent laser field $F(t)$, action S is calculated numerically by integrating p_z^2 along the laser polarization,

$$S = \frac{1}{2}p_\rho^2(t - t') + \frac{1}{2}\int_{t'}^{t} p_z^2 dt'', \tag{15}$$

$$p_z = \int_{t'}^{t} F(t'')dt''. \tag{16}$$

We are assuming that the ionized electron is freely propagating in the classical laser field in the absence of the Coulomb field of its parent ion, and this method is numerically exact under this assumption.

A. Results and discussion

The double plateau structure we see in the one-dimensional spectra in Fig. 1 can also be observed from our three-dimensional simulations. In Fig. 4, the squared dipole acceleration $|a(\omega)|^2$ is plotted for the initial states of $1s$ (black), $4s$ (green), and $8s$ (blue) of hydrogen atom as a function of the scaled harmonic order $\omega/(\omega_0 n) \equiv \widetilde{q}$. In these calculations, we adhere to $\gamma = 0.75$ as in the one-dimensional calculations, and start at $n = 1$ with intensity 2×10^{14} W/cm^2 and $\lambda = 800$ nm. From this, we use the n scaling discussed in Sec. II to determine the laser parameters for higher n states. Apart from the double plateau structure, there is a decrease in the HHG yield with increasing n in Fig. 4, similar to the one-dimensional case. Again, this suggests that although γ is fixed for all three initial states in Fig. 4, the atom sinks deeper into the tunneling regime as n is increased, similar to what we have seen in the one-dimensional case in Sec. II. The main difference in Fig. 4 is that the first plateau is not as flat as in the one-dimensional calculations, as is often the case when comparing one- and three-dimensional HHG spectra.

In order to clearly identify the first and the second cutoffs seen in Fig. 1, we have smoothened the $4s$ and $8s$ spectra by boxcar averaging to reveal their main structure (solid red curves) in Fig. 4. The usual scaled cutoff from the semiclassical three-step model is at $q_{\max}/n \simeq 35$ in all three spectra, and it is independent of n. A secondary cutoff emerges at the same scaled harmonic as in the one-dimensional case, which is labeled as k_2 in the $4s$ and the $8s$ spectra at $\widetilde{q} \simeq 23.45$. It is clear from Fig. 4 that just as the usual cutoff at $q_{\max}/n$, k_2 is also universal beyond $n > 4$. This secondary cutoff separates the two plateaus, first spanning lower frequencies below k_2, and the second spanning higher frequencies between k_2 and $q_{\max}/n$.

The mechanism behind the formation of the secondary cutoff k_2 can be understood in terms of the ionization and the recombination steps of the semiclassical model. In the first step, the electron tunnels out of the initial ns state into the continuum, and has initially no kinetic energy. After excursion in the laser field, it recombines with its parent ion. In this last step, recombination occurs primarily back into the initial state. This is because the electron was liberated into the continuum with virtually no excess kinetic energy, and the electron wave packet mainly retains its original character. When it returns to its parent ion to recombine, the recombination probability is highest for the bound state with which it overlaps the most. As a result, recombination into the same initial state is favored. This mechanism is associated with the usual cutoff since its position depends on the ionization potential: $q_{\max} = (I_p + 3.17U_p)/\omega_0$.

On the other hand, there is still a probability that the electron can recombine to higher n states. This would result in lower harmonics because less than I_p needs to be converted to harmonics upon recombination. The cutoff for this mechanism would be achieved when the electron recombines with zero energy near the threshold ($n \to \infty$). Because the maximum kinetic energy a free electron can accumulate in the laser field is $3.17U_p$, the lower harmonic plateau would cut off at $3.17U_p$. For the laser parameters used in Fig. 4, this corresponds to the scaled harmonic $\widetilde{q} = 23.45$, which is marked by the red arrows labeled as k_2 on the $4s$ and the $8s$ spectra. To reiterate, the second plateau with higher harmonics includes (1) trajectories which recombine to the initial state ($n_1 \to n_1$) after accumulating kinetic energy up to $3.17U_p$; (2) trajectories which recombine to a higher but nearby n state ($n_1 \to n_2$, where $n_2 > n_1$) that have acquired kinetic energy up to $3.17U_p$; and (3) trajectories which recombine to much higher n states ($n_1 \to n_2$, where $n_2 \gg n_1$) resulting in the cutoff at $\widetilde{q} = 23.45$.

The n and l distributions for the $4s$ and $8s$ states as a function of time can be seen in Fig. 5. Notice that the laser pulse is centered at $t = 0$ o.c. and has four cycles at FWHM for both states. It is clear from the first column that the the atom

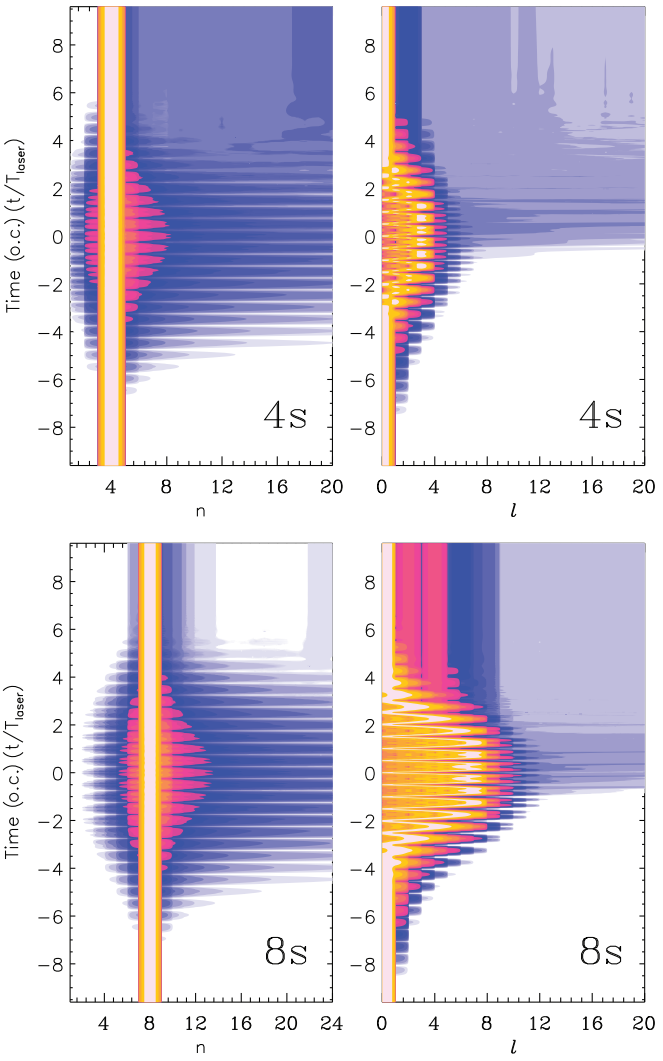

FIG. 5. (Color online) n and l distributions for the probability to find the atom in $4s$ and $8s$ states of H for the laser parameters used in Fig. 4. All probabilities are plotted in $\log_2$ scale and the lowest contour in the n distributions for both states is at the 10^{-10} level. The half-cycles of the four-cycle laser pulse are clearly visible.

mostly stays in the initial state and only a small fraction of the wave function contributes to the HHG process. To appreciate how small, we note that the highest contour is at unity, and the lowest contour for both the $4s$ and the $8s$ states are at the $\sim 10^{-10}$ level. At the end of the pulse, there is a small spread in n, which is skewed towards higher n in both cases. This skew is expected since the energy separation between the adjacent n manifolds drop as $\sim 1/n^3$, and therefore it is easier to spread to the higher n manifolds than to lower n. The small amplitude for this spread is a consequence of the fact that we are not in the n-mixing regime. In the second column, we see that the orbital angular momentum l also spreads to higher l within the initial n manifold, and the small leakage to higher angular momenta at the end of the pulse is a consequence of the small probability for spreading to the higher n manifolds.

The second step of the harmonic generation process involving the free evolution of the electron in the laser field can be understood on purely classical grounds. It was the classical

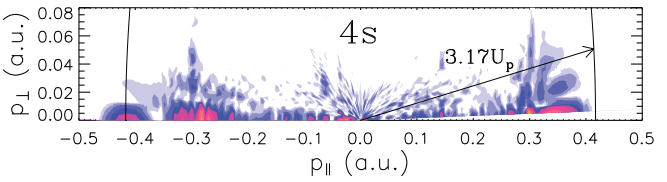

FIG. 6. (Color online) The momentum distribution for the ionized part of the wave function integrated over time until after the laser pulse when the atom is initially prepared in the $4s$ state. The total momentum $\sqrt{p_\parallel^2 + p_\perp^2}$ corresponding to the maximum kinetic energy that can be attained by a free electron in a laser field is marked by the dot-dashed semicircle and labeled as $3.17U_p$. This is the limit that determines the semiclassical cutoff at $q_{\max} = I_p + 3.17U_p$.

arguments that led to the $3.17U_p$ limit for the maximum kinetic energy attainable by a free electron. In the context of this paper, performing such classical simulations can yield no insight into how the excursion step of the HHG behaves under the scaling scheme we have employed so far. This is because the classical equations of motion perfectly scale under the transformations $r \to rn^2$, $t \to tn^3$, $\omega \to \omega/n^3$, and $E \to E/n^2$, where r is distance and t is time. On the other hand, it is the lack of this perfect scaling property of the Schrödinger equation that accounts for the differences between different initial n states we have seen from our quantum simulations. One way to examine the excursion step by itself in our quantum simulations is to look at the momentum distribution of the part of the wave function that contributes to the HHG spectra.

To this end, we calculate the momentum map of the ionized part of the wave function when the atom is initially prepared in the $4s$ state. The reason we look at the ionized part of the wave function is because harmonic generation and ionization are competing processes. Therefore one would expect that they should mirror each other in their behavior. Figure 6 shows this momentum distribution obtained by Fourier transforming the ionized part of the wave function, which is accumulated over time until after the laser pulse [see Eq. (12) onward]. Since the problem has cylindrical symmetry, the horizontal axis is labeled $p_\parallel$ to refer to the momentum component parallel to the laser polarization direction (same as p_z). The vertical axis $p_\perp$ is the perpendicular component. We have also labeled the $3.17U_p$ limit for the maximum kinetic attainable, which is along the dot-dashed semicircle. As expected, the total momentum of the escaped electrons cut off at $3.17U_p$, and the components which would have contributed to the two different plateaus in Fig. 4 are visible close to the laser polarization direction.

We also look at the momentum map of the wave function inside our numerical box that falls beyond the peak of the depressed Coulomb potential at $r = 1/\sqrt{F}$. Part of the wave function in the region $r < 1/\sqrt{F}$ is removed by multiplying it with a smooth mask function before the Fourier transformation step described in Sec. III. The results when the atom is initially in the $4s$ and $8s$ states are seen in Fig. 7 at five instances during the laser cycle at the peak of the pulse (labeled A, B, C, D, and E). We have also labeled three semicircles corresponding to three momenta $\sqrt{p_\parallel^2 + p_\perp^2}$ of interest:

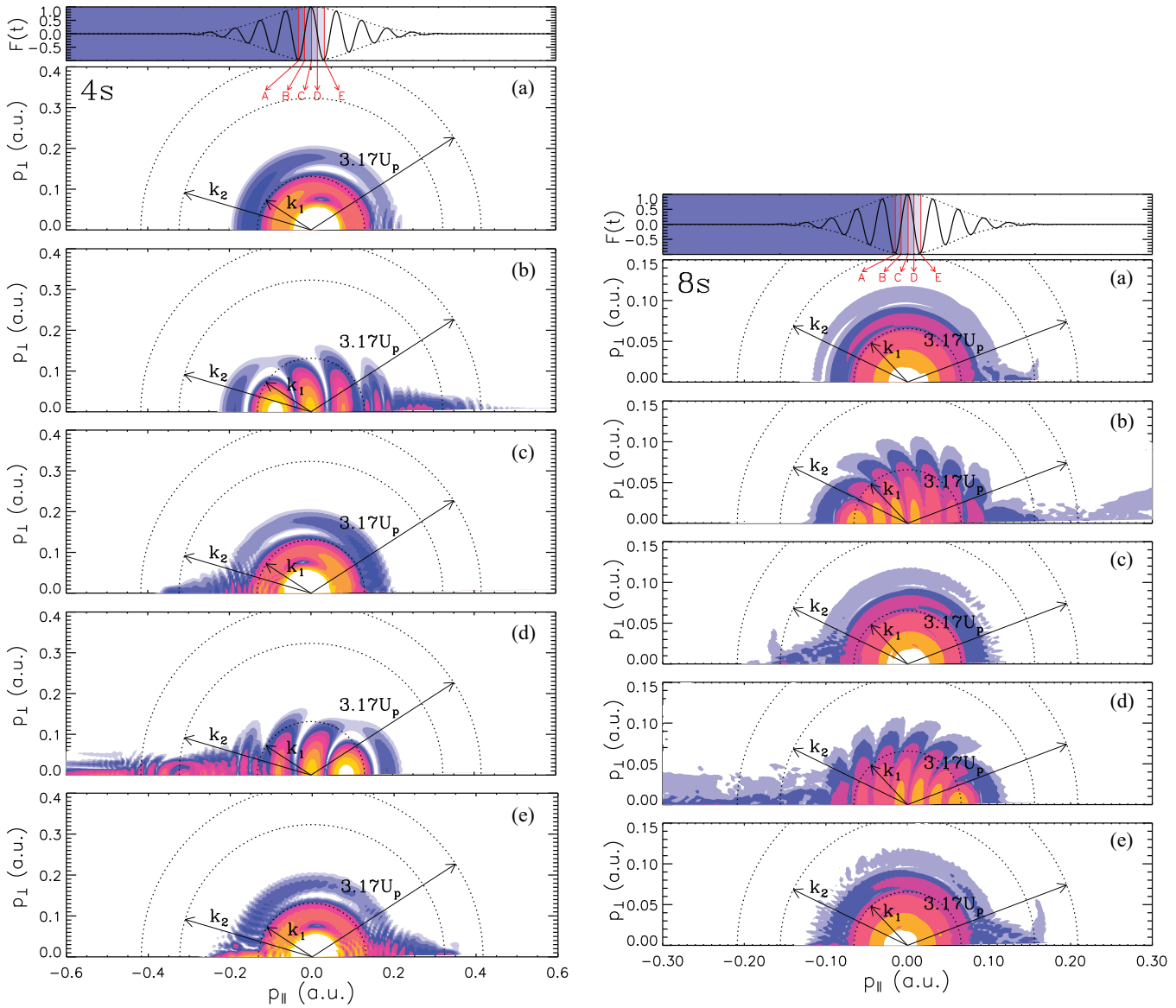

FIG. 7. (Color online) Momentum distributions in the region $r > 1/\sqrt{F}$ for the $4s$ (left column) and $8s$ (right column) states at five instances during the laser cycle at the peak of the pulse (indicated on top). The region $r > 1/\sqrt{F}$ is beyond the peak of the Coulomb potential depressed by the strong laser field.

(1) the $3.17U_p$ limit, also seen in Fig. 6;

(2) k_1 corresponding to the kinetic energy U_p; and

(3) k_2 corresponding to the kinetic energy necessary to emit the harmonic $\widetilde{q} = 23.45$ at the secondary cutoff in Fig. 4, *if the electron recombines into its initial 4s or 8s state upon rescattering*.

Almost all amplitude in Fig. 7 is contained within the k_1 semicircle. The amplitude inside this semicircle contributes to only very low harmonics, below the scaled harmonic labeled as k_1 in Fig. 4. This suggests that the spatial region $r > 1/\sqrt{F}$, which is traversed by long electron trajectories, contributes to only very low harmonics below the first plateau in Fig. 4. The annular region between the semicircles k_1 and the k_2 in Fig. 7 contributes to the first low harmonic plateau, and the region between k_2 and the semiclassical $3.17U_p$ limit contributes to the less intense second plateau in Fig. 4. Since these regions in momentum space include very little amplitude (note that the contours in Fig. 7 are in logarithmic scale), we can conclude that the entire first and second plateaus result from the short trajectories inside the region $r < 1/\sqrt{F}$. This is in agreement with results reported in [21] for ground-state atoms.

Expectedly, both momentum maps for the $4s$ and the $8s$ initial states show the same structures, the essential difference being the number of nodes in the momentum space wave functions inside the k_1 semicircle, which is roughly n. Incidentally, a rescattering event is visible on the laser polarization axis at k_2 in panel (d) of the $4s$ column, giving rise to kinetic energy beyond the $3.17U_p$ limit on the left.

Contributions from the short and long electron trajectories can be separated in the HHG spectra. To this end, we mask the

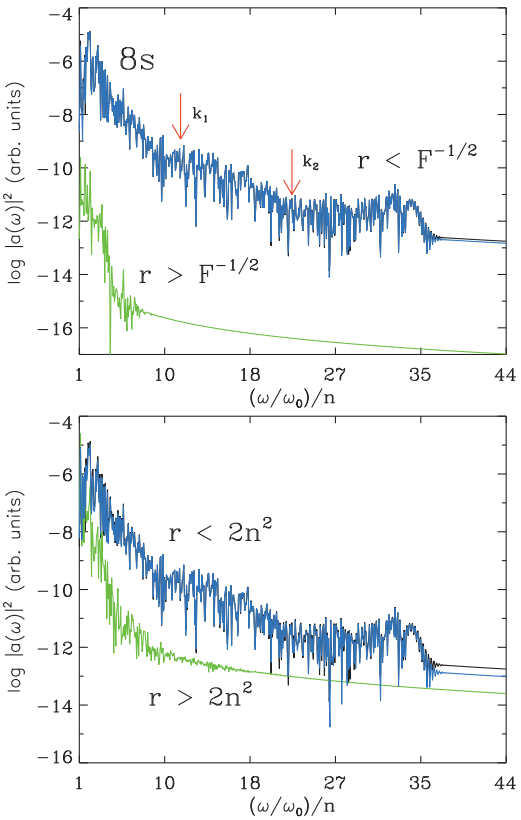

FIG. 8. (Color online) Contributions to the HHG spectrum from the small- and large-r regions when the atom is initially prepared in the8s state. The region $r > 1/\sqrt{F}$ is beyond the peak of the Coulomb potential depressed by the strong laser field at ∼233 a.u., and $2n^2$ is the classical turning point at 128 a.u. for $n = 8$. Both panels show spectra generated using the entire wave function (black curve, same as in Fig. 4), along with the spectra obtained in the $r > r_c$ (green) and $r < r_c$ (blue) regions, where $r_c = 1/\sqrt{F}$ in the upper panel and $r_c = 2n^2$ in the lower panel.

spatial components of the wave function in regions $r < 1/\sqrt{F}$ and $r > 1/\sqrt{F}$ by multiplying it by a mask function which smoothly transitions between these regions. The function $m_t(r)$ masking the $r < 1/\sqrt{F}$ region is the same function used in generating the momentum distributions in Fig. 7, and the function masking the $r > 1/\sqrt{F}$ region is $1 - m_t(r)$. The resulting spectra for the 8s initial state can be seen in the upper panel of Fig 8. For reference, the figure includes the full spectrum for the 8s state from Fig. 4 (black) along with the spectra obtained by masking the $r < 1/\sqrt{F}$ (blue) and $r > 1/\sqrt{F}$ (green) regions. It is clear that the large-r region only contributes to very low harmonics below the U_p limit marked as k_1, whereas the small-r region accounts for the entire range of harmonics. This is in agreement with our discussion of the momentum distributions above, and with previous work involving ground-state atoms [21]. The bottom panel of Fig. 8 shows the spectra when the small- and large-r regions are defined with respect to the classical turning point. Because the turning point is more inland than the peak of the Coulomb potential, the trajectories in the $r > 2n^2$ region account for a wider range of harmonics than the ones inside $r > 1/\sqrt{F}$. This also shows that both plateaus are formed by short trajectories which live well below the turning point.

IV. CONCLUSIONS

We have presented results from one- and three-dimensional time-dependent quantum calculations for higher-order-harmonic generation from excited states of the H atom for a fixed Keldysh parameter γ. Starting from the ground state, we chose laser intensity and frequency such that we are in the tunneling regime and ionization probability is well below 1%. We then scale the intensity by $1/n^8$ and the frequency by $1/n^3$ to keep γ fixed as we increase the principal quantum number n of the initial state of the atom. Because γ is fixed, the common wisdom is that the dynamical regime which determines the essential physics should remain unchanged in the HHG process as we go up in n of the initial state. Our one-dimensional calculations demonstrate that this is indeed the case, and although the emitted power (HHG yield) drops as we climb up in n, the resulting harmonic spectra display same *universal* features beyond $n \sim 10$. The most distinguished feature that develops when the atom is initially prepared in a Rydberg state is the emergence of a secondary plateau below the semiclassical cutoff $q_{\max}$ in the HHG plateau. This secondary cutoff splits the harmonic plateau into two regions: one spanning low harmonics and terminating with a secondary cutoff, and a second plateau with lower yield and higher harmonics terminating at the usual semiclassical cutoff at $q_{\max}$.

We have also found that the positions of these cutoff harmonics scale as $1/n$, and introduced the concept of "scaled harmonic order," $\widetilde{q} = \omega/(\omega_0 n)$. When plotted as a function of $\widetilde{q}$, the harmonic spectra appear universal and, except for the overall yields, the spectra for high n look essentially identical.

We then carried out fully three-dimensional calculations for three of the n states in the lowest n group in the one-dimensional calculations to gain further insight into the scaling properties we have seen in the one-dimensional calculations. This also serves to investigate possible effects of having angular momentum. We found the same features as in the one-dimensional spectra, except that the yield from the first plateau is skewed towards lower harmonics. We associate this with spreading to higher n states during the tunnel ionization and recombination steps by analyzing the n and l distributions of the atom after the laser pulse. Momentum distributions of the ionized electrons show features which we can relate to the universal features seen in the HHG spectra at high n. We further investigate the momentum distribution of the wave function itself beyond the peak of the depressed Coulomb potential at $r = 1/\sqrt{F}$ at various instances during the laser pulse. We find that this region of space, traversed by the long trajectories, contributes only to very low harmonics below the first plateau, which is in agreement with previous results for HHG from ground-state atoms [21]. We identify the first plateau in the HHG spectrum with electrons with kinetic energy between: (1) U_p and (2) the kinetic energy if the electron emits the secondary cut-off harmonic upon recombining to its initial state. The latter case also occurs when the electron recombines to a much higher

Rydberg state than the one it tunnels out after accumulating a maximum possible kinetic energy of $3.17U_p$ during its excursion in the laser field. We further calculate contributions to the HHG spectra due to the short and long trajectories for the $8s$ initial state, which confirms our observation that the region $r > 1/\sqrt{F}$ contributes only to the very low harmonics below the first plateau as reported in [21] for ground-state atoms.

ACKNOWLEDGMENTS

I.Y., E.A.B., and Z.A. were supported by BAPKO of Marmara University. Z.A. would like to thank the National Energy Research Scientific Computing Center (NERSC) in Oakland, CA. T.T. was supported by the Office of Basic Energy Sciences, US Department of Energy, and by the National Science Foundation Grant No. PHY-1212482.

[1] M. Hentschel, R. Kienberger, Ch. Spielmann, G. A. Reider, N. Milosevic, T. Brabec, P. B. Corkum, U. Heinzmann, M. Drescher, and F. Krausz, Nature (London) **414**, 509 (2001).

[2] H. J. Wörner, J. B. Bertrand, D. V. Kartashov, P. B. Corkum, and D. M. Villeneuve, Nature (London) **466**, 604 (2010).

[3] J. Itatani, J. Levesque, D. Zeidler, H. Niikura, H. Pepin, J. C. Kieffer, P. B. Corkum, and D. M. Villeneuve, Nature (London) **432**, 867 (2004).

[4] M.-C. Chen, P. Arpin, T. Popmintchev, M. Gerrity, B. Zhang, M. Seaberg, D. Popmintchev, M. M. Murnane, and H. C. Kapteyn, Phys. Rev. Lett. **105**, 173901 (2010).

[5] M. Rini, R. Tobey, N. Dean, J. Itatani, Y. Tomioka, Y. Tokura, R. W. Schoenlein, and A. Cavalleri, Nature (London) **449**, 72 (2007).

[6] R. L. Sandberg, D. A. Raymondson, C. La-o-vorakiat, A. Paul, K. S. Raines, J. Miao, M. M. Murnane, H. C. Kapteyn, W. F. Schlotter, Opt. Lett. **34**, 1618 (2009).

[7] R. I. Tobey, M. E. Siemens, O. Cohen, M. M. Murnane, H. C. Kapteyn, and K. A. Nelson, Opt. Lett. **32**, 286 (2007).

[8] J. Itatani, F. Quéré, G. L. Yudin, M. Y. Ivanov, F. Krausz, and P. B. Corkum, Phys. Rev. Lett. **88**, 173903 (2002).

[9] P. B. Corkum, Phys. Rev. Lett. **71**, 1994 (1993).

[10] L. V. Keldysh, Sov. Phys. JETP **20**, 1307 (1965).

[11] H. R. Reiss, Phys. Rev. Lett. **101**, 043002 (2008).

[12] H. R. Reiss, Phys. Rev. A **82**, 023418 (2010).

[13] T. Topcu and F. Robicheaux, Phys. Rev. A **86**, 053407 (2012).

[14] S. X. Hu, L. A. Collins, Phys. Rev. A **69**, 033405 (2004).

[15] Z. Zhai, Q. Zhu, J. Chen, Z. C. Yan, P. Fu, and B. Wang, Phys. Rev. A **83**, 043409 (2011).

[16] Z. Zhai, J. Chen, Z.-C. Yan, P. Fu, and B. Wang, Phys. Rev. A **82**, 043422 (2010).

[17] Z. Zhai, Liu X-shen, J. Phys. B **41**, 125602 (2008).

[18] T. Topcu and F. Robicheaux, J. Phys. B **40**, 1925 (2007).

[19] A. D. Bandrauk, S. Chelkowski, D. J. Diestler, J. Manz, and K.-J. Yuan, Phys. Rev. A **79**, 023403 (2009).

[20] Y. Ni, S. Zamith, F. Lepine, T. Martchenko, M. Kling, O. Ghafur, H. G. Muller, G. Berden, F. Robicheaux, and M. J. J. Vrakking, Phys. Rev. A **78**, 013413 (2008).

[21] K.-J. Yuan and A. D. Bandrauk, Phys. Rev. A **80**, 053404 (2009).